

Dynamical simulations of stress, strain, and finite deformations

M. W. Ribarsky and Uzi Landman

School of Physics, Georgia Institute of Technology, Atlanta, Georgia 30332

(Received 31 May 1988)

Formulations and methodologies of molecular-dynamics simulations of material systems evolving under applied finite external perturbations are developed and discussed. Focusing on interfacial systems, composed of interfacing crystalline solids characterized by differing interatomic interactions and atomic sizes, the mechanisms and dynamics of response and stress relief in the elastic, plastic, and inelastic regimes are investigated. Critical values of the external perturbations (stress and strain) are determined, showing dependence on the nature of the interface and the ambient conditions (thermally adiabatic versus isothermal).

I. INTRODUCTION

Basic understanding of the structure and dynamics of materials and their properties often requires knowledge on a microscopic level of the underlying energetics and interaction mechanisms whose consequences we observe and measure. The structural, mechanical, and dynamical response of material systems to external stresses, on the atomic level, are key issues in developing a fundamental understanding of a number of systems and phenomena of coupled basic and technological interest such as tribology, lubrication, wear, material fatigue and yield, crack propagation, stress-induced phase and structural transformations, and hydrodynamical phenomena, to name just a few. Although the above-listed phenomena represent everyday experiences and have been observed and studied for a long time, detailed microscopic theories of them (with few exceptions) are lacking. Nevertheless large bodies of empirical data and in some cases phenomenological model descriptions have been developed.

Common observations related to the above phenomena, and of thermomechanical properties and response of materials in general, are usually made at the continuum level.¹ Consequently (and naturally) the development of theoretical understanding of these phenomena followed the "continuum modeling" approach.¹ The methodology of the development of these models is based on the principles of mass, momentum, and energy balance, and the formulation of constitutive equations. While the mathematical formulation of classical models of the mechanical response of matter (such as the classical theories of elasticity and hydrodynamics) achieved a high degree of sophistication, current focus is on the incorporation of the knowledge about the microscopic behavior of materials in continuum models which attempt to describe macroscopic observations. This is done via the introduction, into the continuum models, of a set of state variables which provide averaged (coarsened) representations of the relevant microscopic quantities. In addition we should note that most applied models of mechanical response are limited to the elastic (small spatial deformation) and linear (small rates of application of the external

perturbation) regimes. Attempts to incorporate inelastic response and nonlinear effects result in a great (often prohibitive) complexity.

Computer molecular-dynamics (MD) simulations²⁻⁹ where the evolution of a physical system is simulated, with refined temporal and spatial resolution, via a direct numerical solution to the model equations of motion are in a sense computer experiments which open new avenues in investigations of the microscopic origins of material phenomena. These methods alleviate certain of the major difficulties which hamper other theoretical approaches, particularly for complex systems such as those characterized by a large number of degrees of freedom, lack of symmetry, nonlinearities, and complicated interactions. In addition to comparisons with experimental data, computer simulations can be used as a source of physical information which is not accessible to laboratory experiments, and in some instances the computer experiment itself serves as a testing ground for theoretical concepts.

At this stage, the development and application of computer simulations to studies of materials phenomena, and in particular the mechanical, structural, and dynamical response of materials to external perturbations, can be used in order to investigate the microscopic mechanisms of material response and to determine the critical material parameters (cohesive energies, interaction potentials, atomic sizes, crystallographic structure) and ambient conditions (for example, thermally adiabatic versus isothermal conditions and dependencies on the strength and rate of applied external perturbations) which govern the observed trends. The information which can be obtained via microscopic simulations could then guide the formulation of continuum models, provide numerical values for certain physical material characteristic parameters which could be incorporated in such models, and provide guidance for the design and analysis of well-controlled experimental investigations.

Traditionally, MD simulations have been employed in studies of systems of fixed shape and size of the periodically replicated calculational cell (i.e., constant volume simulations). More recently methods for simulating systems in which the volume and shape of the calculational

cell may vary dynamically have been developed,^{10–15} opening the way to investigations of a large number of materials phenomena in which the dynamical freedom of the system to change volume and/or structure (or phase) is essential.¹⁵ In addition, a number of methods have been developed for simulations of flow and hydrodynamical systems,^{16–19} which allow detailed investigations of these nonequilibrium phenomena. Using molecular-dynamics techniques various studies of the mechanical properties of solids and fluids have been reported. Among the investigations of solid systems we note studies of stressed solids and crack propagation,^{20–25} dislocation energetics and dynamics,²³ structural transformations in crystal lattices under uniaxial tension or compression,^{11,15,26,27} sliding and migration of grain boundaries,¹⁵ simulations of plastic deformations and shock wave dynamics,^{28,29} studies of stressed interfaces,¹⁷ and calculations of elastic coefficients using MD simulations.³⁰

In this paper we investigate, using MD simulations the microscopic dynamical response, deformation, and stress-relief mechanisms at crystalline solid interfaces subject to externally applied perturbations. Studies of solid interfaces are of inherent as well as applied interest in the development of atomistic models of friction, solid lubrication, and wear phenomena, since plastic deformation which occurs in the vicinity of the interface between sliding materials is the principal mechanism for the dissipation of frictional work.¹ The objectives of these studies are (i) identification of the mechanisms for solid interfacial systems of deformation, stress accumulation and relief, and the dynamical response to external perturbations, (ii) identification of the dependence of the above phenomena on material characteristics, such as bonding strength, atomic sizes, and interface crystallography, and on ambient conditions (thermally adiabatic versus isothermal), and (iii) the development and critical assessment of MD simulation methods for investigations of the above phenomena. In Sec. II we discuss molecular-dynamics methodologies and techniques for simulations of finite deformations of material systems under stress. The setup of the systems and results of simulations using MD simulation methods, under several thermally adiabatic and isothermal conditions and for systems of different sizes and material characteristics are described and compared in Sec. III. A summary of our findings is given in Sec. IV.

II. MOLECULAR-DYNAMICS FORMULATION

In the molecular-dynamics (MD) method the equations of motion for a set of interacting particles are integrated numerically and properties of the system are obtained from the generated phase-space trajectories of the system.^{2–9} In the case of an extended system periodic boundary conditions (PBC's) are imposed while in simulations of finite aggregates⁶ no such device is used. The starting point of a MD simulation is a well-defined microscopic description of the physical system, in terms of a Hamiltonian or a Lagrangian from which the equations of motion are derived. In the early applications of the MD method to extended systems the simulations were

performed in the microcanonical (E, V, N) ensemble, i.e., the energy E , volume V , and number of particles N in the calculational cell (which is periodically repeated) are constants. The desire to investigate physical situations in which the volume and shape (geometry) of the material system may vary (in response to an external pressure or applied stress) as well as circumstances where isothermal (i.e., constant temperature T) pertain, motivated the development of new MD formulations, such as the ansatz Lagrangian,^{10–13} constrained dynamics,^{4,9} and the Nose-dynamics methods.⁹ In the following we review first the ansatz-Lagrangian method, as extended by Parrinello and Rahman¹¹ (PR) for calculations of systems under externally applied stresses, and its extensions to treat finite deformations.¹² Subsequently we discuss an alternative method for dynamical studies of deformations in which the system evolves under an imposed constant-strain rate. Finally, we describe a variant of the MD method for finite deformation studies and a general method which is particularly suited for investigations^{2,18,19} of systems in which flow phenomena may occur.

A. The ansatz-Lagrangian method: The (\mathcal{H}, τ, N) ensemble

In the PR formulation¹¹ the particles' coordinate vectors whose components are $r_{i\alpha}$ (where $i = 1, 2, \dots, N$ is a particle index and $\alpha = 1, 2, 3$ is a coordinate index) are expressed in terms of scaled coordinate vectors $s_{i\alpha}$ (where $0 \leq s_{i\alpha} \leq 1$, $i = 1, 2, \dots, N$ and $\alpha = 1, 2, 3$) and a matrix \underline{H} whose columns \mathbf{H}_1 , \mathbf{H}_2 , and \mathbf{H}_3 are the vectors $\mathbf{A}, \mathbf{B}, \mathbf{C}$ which span the edges of the MD calculational cell,

$$r_{i\alpha} = \sum_{\beta=1}^3 H_{\alpha\beta} s_{i\beta} \quad (i = 1, 2, \dots, N; \alpha, \beta = 1, 2, 3). \quad (1)$$

The volume of the cell, Ω , is given by $\det(\underline{H}) \equiv | \underline{H} |$.

Regarding the components of the \underline{H} matrix as dynamical variables, Parrinello and Rahman¹¹ have originally proposed a Lagrangian (a Hamiltonian formulation can also be developed^{12,27}) from which the equations governing the time evolution of the $3N + 9$ degrees of freedom ($3N$ particle and nine calculational cell degrees of freedom) are obtained:

$$L_{\text{PR}} = \frac{1}{2} \sum_{i=1}^N [m_i \dot{s}_i^T \underline{G} \dot{s}_i - U(\{\underline{H}\mathbf{s}_i\})] + K_{\text{cell}} - U_{\text{cell}}, \quad (2)$$

where dotted variables indicate differentiation with respect to time, the superscript T denotes a transpose, the metric tensor \underline{G} is defined as $\underline{G} = \underline{H}^T \underline{H}$, U is the potential energy of the particles (which depends on the specific form of the interparticle interaction), and the cell kinetic energy was chosen by PR as

$$K_{\text{cell}} = \frac{1}{2} W \text{Tr}(\dot{\underline{H}}^T \dot{\underline{H}}), \quad (3)$$

where W is a mass parameter. For the case of a system to which an external stress, specified by the stress tensor $\underline{\sigma}_e$, is applied the potential energy, U_{cell} , is given by

$$U_{\text{cell}} = \Omega_0 \text{Tr}(\underline{\sigma}_e \underline{\epsilon}), \quad (4)$$

where the strain tensor $\underline{\epsilon}$ can be written in terms of the metric tensor \underline{G} and the reference value, \underline{H}_0 , of \underline{H} , in the form

$$\underline{\epsilon} = \frac{1}{2}[(\underline{H}_0^{-1})^T \underline{G} \underline{H}^{-1} - \mathbf{1}] . \quad (5)$$

Using Eq. (5) in Eq. (4), and denoting by $P_e \equiv \frac{1}{3}\text{Tr}(\underline{\sigma}_e)$ the external hydrostatic pressure, the expression for U_{cell} in the small-strain limit¹¹ [i.e., $\text{Tr}(\underline{\epsilon}) \simeq (\Omega - \Omega_0)/\Omega_0$] is

$$U_{\text{cell}} = P_e(\Omega - \Omega_0) + \frac{1}{2}\text{Tr}(\underline{\Sigma} \underline{G}) , \quad (6)$$

where

$$\underline{\Sigma} = \Omega_0 \underline{H}_0^{-1}(\underline{\sigma}_e - P_e \mathbf{1})(\underline{H}^{-1})^T \quad (7)$$

and $\Omega_0 = \det(\underline{H}_0)$. Note that for the case of an isotropic external stress $\underline{\Sigma} = 0$, the second term in Eq. (6) vanishes and only the contribution from the hydrostatic pressure, P_e , remains.

The equations of motion which are derived in the usual manner from the above Lagrangian [Eq. (2)] for the particles are

$$m_i \ddot{\mathbf{s}}_i = - \sum_{j=1}^N \chi_{ij}(\mathbf{s}_i - \mathbf{s}_j) - m_i \dot{\underline{G}}^{-1} \dot{\underline{G}} \mathbf{s}_i \quad (i = 1, 2, \dots, N) , \quad (8a)$$

where $\chi_{ij} = r_{ij}^{-1}(\partial U / \partial r_{ij})$, and those describing the dynamical motion of the calculational cell are given by

$$W \dot{\underline{H}} = (\underline{\sigma} - P_e \mathbf{1}) \underline{A} - \underline{H} \underline{\Sigma} , \quad (8b)$$

where \underline{A} is the ‘‘area tensor,’’ $\underline{A} = \Omega(\underline{H}^{-1})^T$ [i.e., $A_{\alpha\beta} = \partial \Omega / \partial H_{\alpha\beta}$], and the elements of the *internal microscopic stress tensor* $\underline{\sigma}$ are given by

$$\sigma_{\alpha\beta} = \Omega^{-1} \left[\sum_{i=1}^N \left[p_{i\alpha} p_{i\beta} / m_i - \sum_{j=i+1}^N \chi_{ij} r_{ij\alpha} r_{ij\beta} \right] \right] \quad (\alpha, \beta = 1, 2, 3) \quad (8c)$$

where $r_{ij} = |\mathbf{r}_i - \mathbf{r}_j|$ and the momentum $\mathbf{p}_i = m_i \underline{H} \dot{\mathbf{s}}_i$.

The above formulation generates an isenthalpic-isostress $(\mathcal{H}, \sigma_e, N)$ ensemble (\mathcal{H} is the enthalpy) with the elastic energy given by [see Eq. (6)]

$$\begin{aligned} E_{el} &= P_e(\Omega - \Omega_0) + \Omega_0 \text{Tr}[(\underline{\sigma}_e - P_e \mathbf{1}) \underline{\epsilon}] \\ &= P_e(\Omega - \Omega_0) + \frac{1}{2} \text{Tr}(\underline{\Sigma} \underline{G}) . \end{aligned} \quad (9)$$

The sum of E_{el} and the particle kinetic and potential energies is a constant of the motion in this formulation.^{11,12}

Two issues raised at this point are (i) the appropriate choice of the reference state \underline{H}_0 ^{11,12} [see Eq. (5)], and (ii) the nonuniqueness¹² of the form for K_{cell} [Eq. (3)]. Considering issue (i) first it is noted that as far as the definition of the strain tensor $\underline{\epsilon}$ [Eq. (5)] is considered the choice of \underline{H}_0 is arbitrary.^{11,12} However, the choice of the reference system is of importance when considering the elastic energy, particularly when *finite deformations* are involved.¹² An expression for the virtual work δE performed in a virtual deformation (i.e., the elastic energy stored in the medium) of a deformable medium, whose volume in the deformed state is Ω , was derived by Mur-

naghan,³¹

$$\delta E \equiv E_{el} = \int_{\Omega} \text{Tr}[(\underline{H}_0 \underline{H}^{-1} \underline{\sigma}_e \underline{H}^{-1T} \underline{H}_0^T) \delta \underline{\epsilon}] d\Omega , \quad (10)$$

with the strain tensor $\underline{\epsilon}$ defined by Eq. (5) and the *unstressed system*, \underline{H}_0 , as the *reference state*. The integral is to be performed over the final state, i.e., stressed body. The ‘‘calculational cell tensors’’ \underline{H}_0 and \underline{H} for the unstressed and stressed system, respectively, occur in Eq. (10) since a position \mathbf{r} in the deformed system relates to the corresponding position \mathbf{r}_0 in the undeformed body via the Jacobian $\underline{H} \underline{H}_0^{-1}$, i.e., $\mathbf{r} = \underline{H} \underline{H}_0^{-1} \mathbf{r}_0$. In the limit of the infinitesimal theory of elasticity Eq. (10) becomes

$$E_{el} = \int_{\Omega} \text{Tr}(\underline{\sigma}_e \delta \underline{\epsilon}) d\Omega . \quad (11)$$

For a uniform system undergoing a *finite deformation* Eq. (10) takes the form

$$E_{el} = \Omega_0 \text{Tr}(\underline{\tau} \underline{\epsilon}) , \quad (12)$$

where the ‘‘thermodynamic tension’’ $\underline{\tau}$, is defined^{31,32} by

$$\underline{\tau} = \frac{\Omega}{\Omega_0} \underline{H}_0 \underline{H}^{-1} \underline{\sigma}_e (\underline{H}^{-1})^T \underline{H}_0^T . \quad (13)$$

For the *infinitesimal* case we obtain

$$E_{el} = \Omega_0 \text{Tr}(\underline{\sigma}_e \underline{\epsilon}) . \quad (14)$$

We emphasize that in Eq. (12) the reference state, \underline{H}_0 , is the *unstressed system*. In Eq. (14) however, the reference state is a system *under stress* and as proposed by PR,¹¹ in this case \underline{H}_0 could be chosen as the average of the stressed system, $\langle \underline{H} \rangle$. Since the thermodynamic tension $\underline{\tau}$ is the quantity appearing in the thermodynamic expressions,^{31,32} e.g., the enthalpy $\mathcal{H} = E + \Omega_0 \text{Tr}(\underline{\tau} \underline{\epsilon})$, where E is the particle energy, Ray and Rahman¹² proposed the isenthalpic-isotension, (\mathcal{H}, τ, N) , ensemble where $\underline{\tau}$ is constant [*but not* $\underline{\sigma}_e$, see Eq. (13)]. For this ensemble the equations of motion for the particles are as given by Eq. (8a) and the equation for \underline{H} [Eq. (8b)] is replaced by

$$W \dot{\underline{H}} = \underline{\sigma} \underline{A} - \underline{H} \underline{\Gamma} , \quad (15a)$$

where

$$\underline{\Gamma} = \Omega_0 \underline{H}_0^{-1} \underline{\tau} (\underline{H}_0^{-1})^T . \quad (15b)$$

In some of the simulations discussed in the next section we have used the (\mathcal{H}, τ, N) ensemble. In the following section we formulate an alternative dynamical simulation method in which the system evolves under a constant-strain rate.

B. Constant-strain-rate simulations

In the constant-strain-rate (CSR) simulations the calculational cell deforms in a *prescribed way at a prescribed constant rate*. In this method only the particle equations of motion need to be solved since the evolution of the calculational box is given, i.e., the components of \underline{H} do not evolve freely. We remark that since for a given deformation (i.e., prescribed strain) the internal stresses, $\underline{\sigma}$, see Eq. (8c), which the system develops (in equilibrium, or steady state in case of flow) in response to the deforma-

tion can be calculated, the CSR and (\mathcal{H}, τ, N) ensemble (see Sec. II A) simulations can be operated “self-consistently” by using these calculated stresses as applied external stresses in simulations where the dynamical evolution of the calculational cell is included^{11,12} (i.e., using the (\mathcal{H}, τ, N) ensemble, or the isoexternal-stress method described in Sec. C). The formulation of the CSR method is facilitated by defining the streaming velocity, \mathbf{u} , as

$$\mathbf{u} = \underline{\dot{H}} \mathbf{s} . \quad (16)$$

Using this definition the strain-rate tensor, $\underline{\dot{\gamma}}$, is given by

$$\underline{\dot{\gamma}} \equiv \nabla \mathbf{u} = (\underline{H}^{-1})^T \underline{\dot{H}}^T . \quad (17)$$

The equations of motion for the particles can be now written [compare to Eq. (8a)] as

$$\underline{\dot{\gamma}} \equiv \nabla \mathbf{u} = (\underline{H}^{-1})^T \underline{\dot{H}}^T . \quad (17)$$

The equations of motion for the particles can be now written [compare to Eq. (8a)] as

$$m_i \underline{\dot{H}} \dot{\mathbf{s}}_i = - \sum_{j=1}^N \chi_{ij} \mathbf{r}_{ij} - (\underline{H}^{-1})^T \underline{\dot{H}}^T \mathbf{p}_i - m_i \underline{\dot{H}} \dot{\mathbf{s}}_i , \quad (18)$$

where the peculiar momentum \mathbf{p}_i is defined by

$$\mathbf{p}_i = m_i \underline{H} \dot{\mathbf{s}}_i , \quad (19a)$$

and

$$\dot{\mathbf{p}}_i = m_i (\underline{\dot{H}} \dot{\mathbf{s}}_i + \underline{H} \ddot{\mathbf{s}}_i) . \quad (19b)$$

Rearranging terms and using Eqs. (19), we write Eq. (18) as

$$\dot{\mathbf{p}}_i = - \sum_{j=1}^N \chi_{ij} \mathbf{r}_{ij} - \underline{\dot{\gamma}} \mathbf{p}_i \quad (20)$$

and

$$\dot{\mathbf{r}}_i = \mathbf{p}_i / m_i + \underline{\dot{\gamma}}^T \mathbf{r}_i . \quad (21)$$

We note that Eq. (20) is the same as the “Doll’s tensor” equation of motion introduced by Evans and Hoover.¹⁶

As discussed by Ray and Rahman,¹² in the ansatz Lagrangian [Eq. (2)], terms involving $\underline{H} \dot{\mathbf{s}}_i$ are omitted. Employing a Hamiltonian formulation these authors derived¹² an alternative equation of motion which includes the $\underline{H} \dot{\mathbf{s}}_i$ terms [see Eq. (2.12) in Ref. 12],

$$m_i \underline{H} \ddot{\mathbf{s}}_i = - \sum_{j=1}^N \chi_{ij} \mathbf{r}_{ij} - m_i \underline{\dot{H}} \dot{\mathbf{s}}_i - 2m_i \underline{H} \dot{\mathbf{s}}_i . \quad (22)$$

For a process in which the system is deformed at a constant strain rate, $\underline{\dot{\gamma}}$ is constant for a Couette geometry (i.e., fluid sheared between two parallel plates held at a fixed distance from one another, see Sec. III C), the term involving $\underline{\dot{H}}$ in Eq. (22) vanishes and using the definitions of $\underline{\dot{\gamma}}$ [Eq. (17)] and the peculiar momentum, \mathbf{p}_i [Eq. (19a)], the above equation of motion becomes

$$\dot{\mathbf{p}}_i = - \sum_{j=1}^N \chi_{ij} \mathbf{r}_{ij} - \underline{\dot{\gamma}}^T \mathbf{p}_i . \quad (23)$$

We remark that this equation involves the transpose of $\underline{\dot{\gamma}}$ [compare to Eq. (20)], and is the same as the local-rest-frame dynamics (“Slod”) equation of motion (transpose of the non-Newtonian dynamics “Doll’s tensor”) suggested and used by Evans and Morris.¹⁶

Thus we observe that for constant-strain rate the equations of motion generated via the Parrinello and Rahman,¹¹ and Ray and Rahman¹² formulations reduce to those used in the nonequilibrium-molecular-dynamics (NEMD) method.¹⁶ In the constant-strain-rate (CSR) simulations described below we have used Eqs. (23), following NEMD studies. However, we remark that simulations employing Eqs. (20) yield qualitatively similar results.

C. Isoexternal-stress formulation

In the previous two sections we discussed methods for molecular-dynamics simulations of system which undergo finite deformations, i.e., the isoenthalpic-isotension, (\mathcal{H}, τ, N) ensemble, and constant-strain-rate (CSR) methods. In order to allow simulations of systems under *constant external stress*, $\underline{\sigma}_e$, we have developed a new method which in addition avoids certain pathological circumstances which may be encountered when using the previous methods, particularly when flow develops. While we do not use this method of simulations in this paper, we include a brief discussion of it for completeness.

In order to develop an isoexternal-stress dynamical method, we consider the Lagrange equations of motion which include nonconservative forces,³³ \mathbf{Q}_i ,

$$\frac{d}{dt} \left[\frac{\partial L}{\partial \dot{q}_{i\alpha}} \right] - \left[\frac{\partial L}{\partial q_{i\alpha}} \right] = Q_{i\alpha} , \quad (24)$$

$$(\alpha = 1, 2, 3)(i = 1, 2, \dots, N + 9) ,$$

where the set of \mathbf{q}_i ’s and $\dot{\mathbf{q}}_i$ ’s include the dynamical degrees of freedom of the particles and of the calculational cell. The virtual work, δE , done by the nonconservative forces is given by

$$\delta E = \sum_i \mathbf{Q}_i \cdot \delta \mathbf{q}_i . \quad (25)$$

Recalling the definition of the area tensor, \underline{A} [see Eq. (8b)] we note that the components ($\mathbf{A}_1, \mathbf{A}_2, \mathbf{A}_3$) of \underline{A} are the areas of the calculational cell times their respective normals (i.e., $\mathbf{A}_1 = \mathbf{H}_2 \times \mathbf{H}_3$, etc.). Therefore due to a virtual deformation of the calculational cell (in which the vectors \mathbf{H}_α are changed by $\delta \mathbf{H}_\alpha$) each of the surfaces \mathbf{A}_α is displaced by $\delta \mathbf{H}_\alpha$. The amount of virtual work done in displacing each of the surfaces due to the force $\underline{\sigma}_e \mathbf{A}_\alpha$ is $\delta \underline{H}^T \underline{\sigma}_e \mathbf{A}_\alpha$ (for $\alpha = 1, 2, 3$). For a general virtual displacement $\delta \underline{H}$ the virtual work done is

$$\delta E = \text{Tr}(\delta \underline{H}^T \underline{\sigma}_e \underline{A}) , \quad (26)$$

which can be shown to be the same as the result given in Eq. (10) for a uniform system. Comparing Eqs. (25) and (26) the Lagrange equations of motion [Eq. (24)] for the calculational cell take the form

$$\frac{d}{dt} \left[\frac{\partial L}{\partial \dot{H}_{\alpha\beta}} \right] - \frac{\partial L}{\partial H_{\alpha\beta}} = \sum_\gamma \sigma_{e,\alpha\gamma}(t) A_{\gamma\beta} \quad (\alpha, \beta = 1, 2, 3) , \quad (27)$$

where we have denoted the q ’s and \dot{q} ’s corresponding to the calculational box by H and \dot{H} and the possible depen-

dence of the external stress tensor, $\underline{\sigma}_e$, on time is indicated. Using the Lagrangian given in Eq. (2), but without the term U_{cell} which is explicitly accounted for in Eq. (27), equations of motion for the calculational cell tensor, \underline{H} can be derived yielding,

$$W\ddot{\underline{H}} = (\underline{\sigma} - \underline{\sigma}_e) \underline{A}, \quad (28)$$

in place of Eq. (8b), or (15a) in the previous formulations. The particle equations of motion remain unchanged [Eq. (8a)]. Note that here $\underline{\sigma}_e$ is *constant* unlike the case of the (\mathcal{H}, τ, N) ensemble equations of motion and that the question of reference state does not arise. The system however is nonconservative.

We turn next to the issue of the nonuniqueness of the form of the calculational cell kinetic energy, K_{cell} [see Eqs. (2) and (3)]. This question has been addressed before and it has been shown that any form for K_{cell} which is a function of H and \dot{H} generates the isoenthalpic-isobaric ensemble for sufficiently large N .¹² Furthermore, note that for such choices the particle equations of motion [Eq. (8a)] are independent of K_{cell} as are also equilibrium equal-time ensemble averages.^{16,12}

It is natural to demand that the equations of motion governing the dynamical evolution of the system will be invariant under transformations connecting equivalent computational cells¹⁹ (which may differ in shape but are of the same volume, and contain equivalent sets of particles). Since $\underline{H} \equiv (\underline{H}_1, \underline{H}_2, \underline{H}_3)$, defining the computational cell, fully incorporates the periodicity of the system, i.e., any two equivalent points in the periodically replicated system may be connected by a vector $n_1 \underline{H}_1 + n_2 \underline{H}_2 + n_3 \underline{H}_3$ where n_1, n_2 , and n_3 are integers, we define¹⁹ the class of transformations under which the system is translationally invariant as T transformations. These transformations have the property that all the elements of the (3×3) transformation matrix \underline{T} are integers and that $\det(T) = 1$ (to assure conservation of volume).

It has been recently shown¹⁹ that previous choices for K_{cell} [such as the Parrinello-Rahman form,¹¹ Eq. (3), and variants thereof¹²] lead to equations of motion for the calculational cell which do not obey the above invariance requirement. Moreover, it has been shown that using K_{cell} given by

$$K_{\text{cell}} = \frac{1}{2} W \text{Tr}(\dot{\underline{H}} \underline{A}^T \underline{A} \dot{\underline{H}}^T), \quad (29)$$

generates equations of motion invariant under T transformations and in addition leads to satisfaction of the virial theorem at equilibrium (where it is appropriate, i.e., isotropic pressure $\underline{\sigma}_e = \frac{1}{3} P_e \underline{1}$).

In addition to providing a more complete description by virtue of obeying a natural invariance requirement, this formulation presents a technical advantage which is of importance particularly in simulations of flow systems.¹⁸ Consider, for example, a fluid flowing under the influence of an external stress under steady-state conditions. For concreteness take the external stress tensor $\underline{\sigma}_e$ to be a symmetric tensor $\sigma_{\alpha\beta} = C(\delta_{\alpha 1} \delta_{\beta 3} + \delta_{\alpha 3} \delta_{\beta 1})$, where C is an arbitrary constant. Under the influence of the external stress the calculational cell will eventually be-

come extremely nonorthogonal (in fact due to the absence of effective resistance to flow, such skewed calculational cell may develop in fluid simulations even without external stresses). Suppose that the interparticle interaction potentials in the system extend to a finite range smaller than the linear dimension of the calculational cell. Then in calculating the force acting on particle i we need to include contributions from all particles located inside the range of interaction in the calculational cell and from their images in the first (so-called minimum image) periodic replications of the cell. As long as the calculational cell does not deviate much from being cubical (i.e., orthogonal) the search for periodic images can be implemented most efficiently by finding the nearest integer to each component of the scaled coordinates [see Eq. (1)], $s_j - s_i$. However, for very skewed cells there is no such efficient procedure and since this segment of the calculation is one of the most time consuming parts of the simulation this poses a serious impediment. A solution to this problem is to transform, in the course of the simulation, the skewed cell to an equivalent one which is more orthogonal, as often as necessary. This transformation involves only the small number of degrees of freedom associated with the calculational cell (\underline{H}). Of course, in order to afford such transformations one must require that the equations of motion governing the system evolution be invariant under these transformations, which is achieved via the choice of K_{cell} given in Eq. (29). Recent simulations in our laboratory¹⁸ of stressed systems beyond the yield point and of sheared fluids support the usefulness of the new method.

III. RESULTS

To investigate the properties and the dynamics, energetics and response of a solid to externally imposed forces we have performed molecular-dynamics simulations on a model system at different ambient conditions. To illustrate the different simulation modes discussed in the previous section we compare results obtained for systems in which the calculational cell was allowed to respond dynamically to an external thermodynamic tension (see Sec. II A) with those obtained for a calculational cell which is deformed (keeping the volume unchanged) at a constant-strain rate (the CSR method described in II B). The two simulation modes illustrate various aspects of the deformation process and the approach of the system to yield. The dynamical cell mode of simulation may be likened to the situation where a load and shear stress are applied to materials in frictional contact, resulting in processes which are accompanied by volume changes, while the constant-strain-rate mode corresponds to experiments in which a material pressed between two parallel moving plates (slabs, which are kept at constant distance) is strained. As the stress on the solid system is increased, or equivalently as the strain is increased, the materials deform, first elastically and then inelastically culminating in yield when a disruption of the material occurs. In this paper we investigate the response of the solid as it approaches the yield point. Studies beyond yield require a modification of the simulation procedure (see Sec. II C) and will be discussed elsewhere.¹⁸

A. System setup

In this study we focus on the mechanisms and dynamics of the response of a system containing an interface between two materials to external stresses. The model system which we employ in our simulations consists of N particles (N_A of type A and N_B of type B , $N_A + N_B = N$) interacting via pairwise 6-12 Lennard-Jones (LJ) potentials

$$V(r) = 4\epsilon_{\alpha\beta} \left[\left(\frac{\sigma_{\alpha\beta}}{r} \right)^{12} - \left(\frac{\sigma_{\alpha\beta}}{r} \right)^6 \right] \quad (\alpha, \beta) = A, B, \quad (30)$$

where A and B represent two types of materials. The solid is set up initially in a face-centered-cubic crystalline structure, with $N_L(111)$ layers (N/N_L particles per layer) with the z axis along the $[111]$ direction,³⁴ and three-dimensional periodic boundary conditions are used (see Fig. 1). The well-depth parameter ($\epsilon_{\alpha\beta}$) of the interaction potential between particles in layers $1-N_{LA}$ is taken to be twice that for particles in layers $N_{LA}+1-N$ (i.e., $\epsilon_{AA} = 2\epsilon_{BB}$) corresponding to a soft, solid, lubricating material (the B system) pressed between hard-material slabs (the A system). In order to isolate the dependence of the system response on the interaction strength (potential depth) parameter, ϵ , from that due to differences in the atomic sizes (and thus interatomic distances) associated with the parameter σ in the LJ potential, we have performed first simulations in which $\epsilon_{AA} = 2\epsilon_{BB}$ and $\sigma_{AA} = \sigma_{BB}$, and then simulations in which $\sigma_{BB} = 1.5\sigma_{AA}$. The interspecies LJ potential parameters were chosen as $\sigma_{AB} = (\sigma_{AA} + \sigma_{BB})/2$ and $\epsilon_{AB} = (\epsilon_{AA}\epsilon_{BB})^{1/2}$. In the following we use reduced units³⁵ where energy and temperature are expressed in units of ϵ_{AA} , length in units of σ_{AA} , stress in units of $(\epsilon_{AA}/\sigma_{AA}^3)$, and the time unit (t.u.) is $(m_A/\epsilon_{AA})^{1/2}\sigma_{AA}$. In the integration of the equations of motion we used a time step $\Delta t = 0.0075$ t.u. where

$$\text{t. u.} = (m_A/\epsilon_{AA})^{1/2}\sigma_{AA},$$

which results in energy conservation (to six significant figures) for extended runs.

In most of our simulations we have used systems consisting of $N = 1260$ particles with 18 (111) layers (N_L) and $N_{LA} = N_{LB} = 9$ (unless specified differently results are for this size systems). However, in order to investigate and assess system size dependencies we have also carried out comparative simulations for systems containing $N = 1890$ particles with $N_{LA} = 9$ (i.e., $N_A = 630$) and $N_{LB} = 18$ (i.e., $N_B = 1260$). Some results from these simulations will be exhibited when the size dependence is discussed.

B. Applied thermodynamic-tension simulations: (\mathcal{H}, τ, N) ensemble

1. Adiabatic conditions

In all our simulations we equilibrate first the initial system at a reduced temperature of $T = 0.11$ (note that a

pure bulk LJ crystal melts at $T \simeq 0.7$, and thus, since $\epsilon_{BB} = \epsilon_{AA}/2$, the bulk melting point of the soft material, B , is half that of the A material). Subsequently we apply to the system a load along the $[111]$ (z) direction (normal to the interface, as shown in Fig. 1) at a rate of $0.0025(\epsilon/\sigma^3)/\Delta t$ until a load value of 0.5 is reached. Following equilibration under this load we apply to the system a thermodynamic tension $\underline{\tau}$ in the $[1\bar{1}0]$ direction (see Fig. 1) at a rate of $\dot{\tau}_{xz} = 0.00125(\epsilon/\sigma^3)/\Delta t$ and follow the evolution of the system until it fails [to keep the system against a rigid rotation a symmetric thermodynamic tension tensor $\underline{\tau}$ is applied (i.e., $\tau_{xz} = \tau_{zx}$)].

To investigate the dependence on the thermal ambient conditions we distinguish between simulations where the system is thermally isolated during the application of the shear [discussed in (1)] and simulations where isothermal conditions are maintained [discussed in (2)]. The temporal history of the applied tension versus time for the adiabatic and isothermal conditions are shown in Figs. 2(a) and 2(b), respectively. As the system evolves under the applied shear it develops internal stresses which are calculated using the positions and forces on the particles using Eq. 8(c). For a rate of increase of the applied external shear which is much smaller than the characteristic relaxation rates of the material the system would evolve on a phase-space trajectory which corresponds to an equilibrium (or quasiequilibrium) path for which the values of the external and internal stresses are equal along the system evolution. For externally applied thermodynamic tension above a certain critical value [τ_c and the corresponding calculated critical external stress σ_{ec} , see Eq. (13)] failure of the system will occur, evidenced by a drop of the internal stresses to zero (i.e., stress relief) and an unbounded variation of the volume of the system. Since the rate of increase of the applied thermodynamic tension, τ , indicated by the solid line (slanted) in Fig. 2, is not slow enough to allow the system to relax at all times, the critical values thus obtained serve only as rough estimates (upper bounds) to the true, quasistatic, critical values. Therefore, to obtain a more accurate estimate of the critical stress we have performed simulations at constant values of the thermodynamic tension indicated by

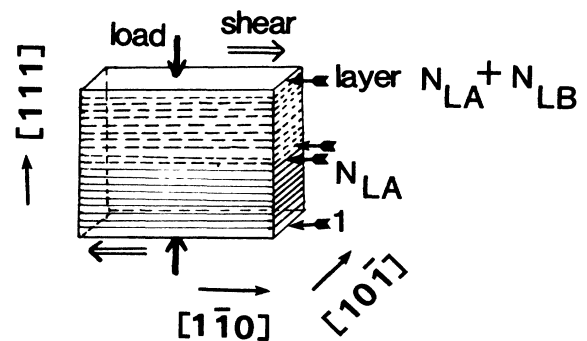


FIG. 1. A schematic of the calculational cell. N_{LA} is the number of layers in the A (hard) material and N_{LB} the number of layers in the B (soft) material. The interface is between layers N_{LA} and $N_{LA} + 1$. The directions of the applied load and shear stresses are indicated. Three-dimensional periodic boundary conditions are employed in the simulations.

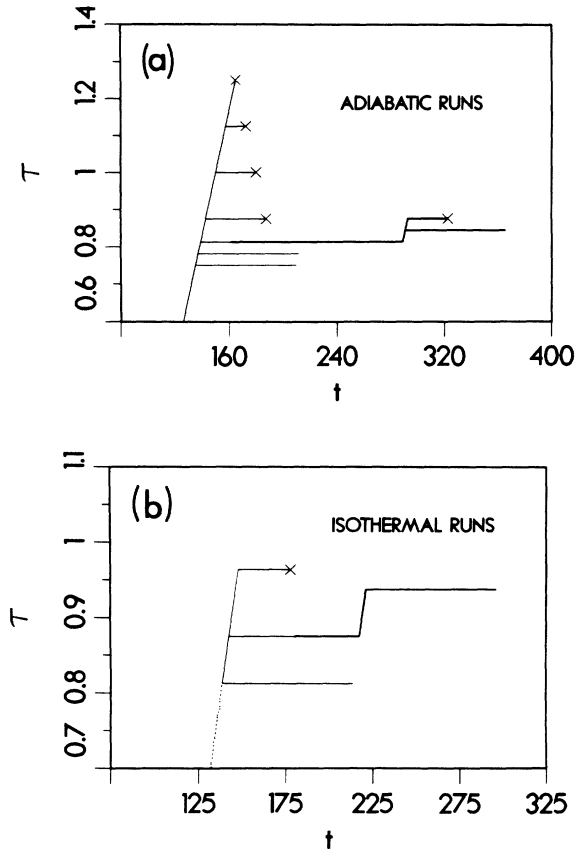


FIG. 2. Summary of the thermally adiabatic (a) and isothermal (b) (\mathcal{H}, τ, N) simulations. The applied thermodynamic tension τ_{xz} vs time (in reduced t.u.) is shown. The slanted solid line represents the rate of application of τ_{xz} (following equilibration under load). Horizontal lines correspond to simulations at constant τ_{xz} , at the values given by the intersection of the lines with the τ axis. The termination of a horizontal line by a symbol (\times) represents that at the corresponding time the system yielded in response to the applied perturbation. Lines which do not terminate by an \times correspond to τ values for which the system did not yield. From these simulations the critical values for structural transformation and eventual yield (given in Table I) were determined. Bold solid lines correspond to the system after slip and stacking-fault formation.

the horizontal solid lines in Fig. 2 (in these simulations the system is brought to the desired value of τ and then evolves under that constant value of the thermodynamic tension). In this figure the absence of a symbol (\times) at the end of a horizontal line indicates that the system did not yield for that value of τ , while a termination of the line by \times indicates yield at the corresponding time. We note that as the value of τ under which the system evolves is increased the time required for the system to yield shortens. The bold solid lines in Fig. 2 correspond to the system after slip and stacking-fault formation. From these simulations we obtain a value of $\tau_{c,xz} = 0.86 \pm 0.02$ for the critical thermodynamic tension (corresponding to $\sigma_{ec,xt} = 0.95 \pm 0.03$), see Table I. Inspection of the real-space trajectories of the particles reveals that yield involves

TABLE I. Critical-yield values of the thermodynamic tension (τ_c), external stress (σ_{ec}), calculated via Eq. (13), and internal stresses (σ_c), calculated via Eq. (8c), obtained from adiabatic and isothermal simulations using the (\mathcal{H}, τ, N) ensemble. The τ_s , σ_{es} , and σ_s values correspond to the critical values of the above quantities for structural transformations prior to yield (stacking fault or slip, as discussed in the text) in the (\mathcal{H}, τ, N) ensemble simulations. Under the constant-strain heading, results are given for the critical strain (γ_s) to bring about an inelastic structural transformation, in constrain-strain simulations, and the corresponding values of the internal stresses, (σ_s) for thermally adiabatic simulations of 18- and 27-layer systems, as well as results for isothermal constant-strain simulations of the 18-layer system. All quantities are in Lennard-Jones reduced units.

	Adiabatic (\mathcal{H}, τ, N)	Isothermal (\mathcal{H}, τ, N)
$\tau_{s,xz}$	0.8 ± 0.02	0.84 ± 0.03
$\sigma_{es,xz}$	0.78 ± 0.01	0.83 ± 0.03
$\sigma_{s,xz}$	0.78 ± 0.01	0.84 ± 0.04
$\tau_{c,xz}$	0.86 ± 0.02	0.95 ± 0.01
$\sigma_{ec,yz}$	0.95 ± 0.03	0.99 ± 0.005
$\sigma_{c,xz}$	0.94 ± 0.02	1.00 ± 0.02
Constant strain		
	Adiabatic (18-layer)	Isothermal (18-layer)
$\gamma_{s,xz}$	0.063 ± 0.002	0.065 ± 0.003
$\sigma_{s,xz}$	0.975	1.02
γ_s / σ_s	0.065	0.064
Adiabatic (27-layer)		
$\gamma_{s,xz}$	0.076 ± 0.002	
$\sigma_{s,xz}$	1.14	
γ_s / σ_s	0.067	

interplanar motion of the (111) atomic layers (relative to one another) in accordance with observations that the main operative slip system in fcc crystals consists of (111) planes in the [110] direction.

For a certain range of values of τ the system undergoes structural transformations which do not result in total yield. This is indicated by the bold solid horizontal lines in Fig. 2 and the corresponding values are given in Table I under $\tau_{s,xz}$ (0.8 ± 0.2 for the adiabatic system and 0.84 ± 0.03 for the isothermal one). To investigate the mechanisms of response and stress relief prior to yield we have performed extensive studies of the behavior of the adiabatic system under an applied $\tau_{xz} = 0.81$. It should be noted that removing the external perturbation prior to the onset of the structural transformation results in the system returning to the average unstressed conditions, while when doing so past the structural transformation the system remains in the deformed state. Records of the average temperature (T), potential energy (E_p), kinetic energy (E_k), and elastic energy (E_{el}) [the work done on the system, see Eq. (12)] versus time (starting at $t = 140$ t.u., the intersection of the horizontal line corresponding to $\tau = 0.81$ with the solid line in Fig. 2) up to the yield point, are shown in Fig. 3. [Note that the sum of the energies in Figs. 3(b)–3(d) is constant.] Inspection of the

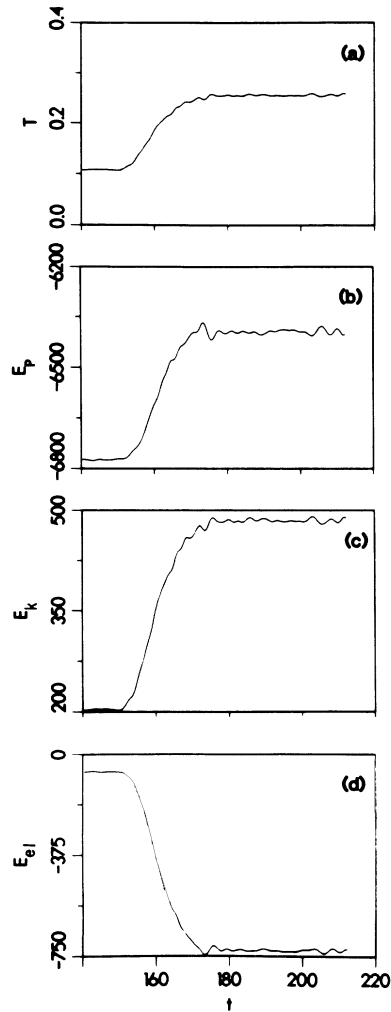


FIG. 3. Records of the temperature (T), potential energy (E_p), kinetic energy (E_k), and elastic energy (E_{el}) vs time (starting at $t=140$ t.u. obtained via an (\mathcal{H}, τ, N) simulation at $\tau_{xz}=0.81$ under thermally adiabatic conditions. The sharp changes in all quantities correspond to structural transformations. All quantities are in Lennard-Jones reduced units.

figures reveals that the average temperature of the system increases from the initial value (in reduced LJ units) of 0.11 achieving a new value of ~ 0.25 at about 175 t.u. Correspondingly, the magnitude of the system average potential energy decreases and the stored elastic energy increase in the above time interval. In addition we find that the volume of the system increases during that time period. Inspection of the structure of the system shows that during the time interval ~ 150 –175 t.u. the system undergoes structural transformations, occurring in the region occupied by the soft (lubricant) material (layers 10–18). The positions of atoms in a central $(11\bar{2})$ slice of the system before and after the transformation displayed in Figs. 4(a) and 4(b), respectively, show clearly the formation of stacking-fault region [i.e., change from the *abcabc* . . . registry sequence, see Fig. 4(a)], in the soft material (open circles). In addition to the formation of the

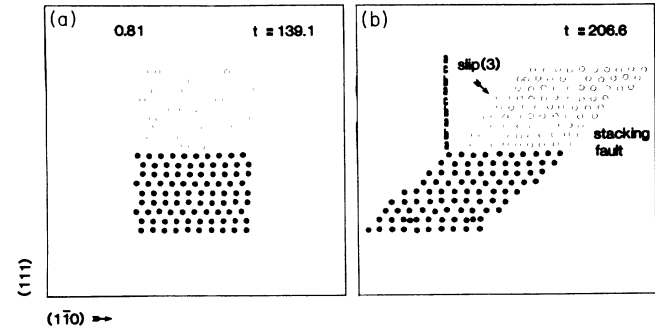


FIG. 4. Atomic trajectories for a $(11\bar{2})$ central slice of the system simulated with $\tau=0.81$: (a) at $t=139.1$ t.u. and (b) at $t=206.6$ t.u., i.e., past the structural transformation (see Fig. 3). As indicated in (b) the structural transformation consists of stacking-fault formations and slip (by three atomic rows).

stacking faults a slip region, where layers 15–18 shifted by three atomic rows to an equivalent registry, is detected. As seen the formation of the stacking fault involves layers 12 and 13. The details of this structural transformation are shown in Fig. 5 where particle positions in layers 12 (solid circles) and 13 (open circles) at three times [before (a), during (b), and after (c)], separated by $170 \Delta t$, are shown.

The mechanical response and energetic characteristics of the system can be investigated best via layer decomposition of the system properties. In Figs. 6(a) and 6(b) we depict the per-layer xz component of the internal stress for the interface layers (layer 5, 8, and 9 of the hard material and layers 10–14 of the soft material). From these figures we observe that the generation of the structural transition involves a gradual decrease in the internal σ_{xz} component in layers 11–14 of the soft material while the variation in the stress in layer 10 [the atomic plane of the soft material (*B*) adjacent to the hard material (*A*), see Fig. 1] is smaller. As seen from Fig. 6(a) the stress relief process and the associated structural transformation in the soft material are accompanied by a stress accumulation in the interfacial region of the hard material (layer 9). In addition we observe periodic oscillations in the internal stress (most pronounced for layers 11–14) past the structural transformation period, as the system relaxes in the new state after the structural transformation events. The energetics of the system is explored via the time records of the per-layer potential energies (E_p') and temperature (T') shown in Figs. 7(a) and 7(b), respectively. From the potential-energy curves we find that the potential energy of particles in layer 11 (second layer from the interface, see Fig. 1) in the soft material is initially lower than that of layers 12–14, which are further removed from the interface, since particles in that layer are within the range of the stronger interaction with the hard substrate [$\epsilon_{AB} = (\epsilon_{AA}\epsilon_{BB})^{1/2}$]. The potential energy of particles in the interfacial soft-material layer (layer 10) adjacent to the hard material is lower by about -0.4ϵ than the value for layer 11, and as seen from Fig. 6(a) the

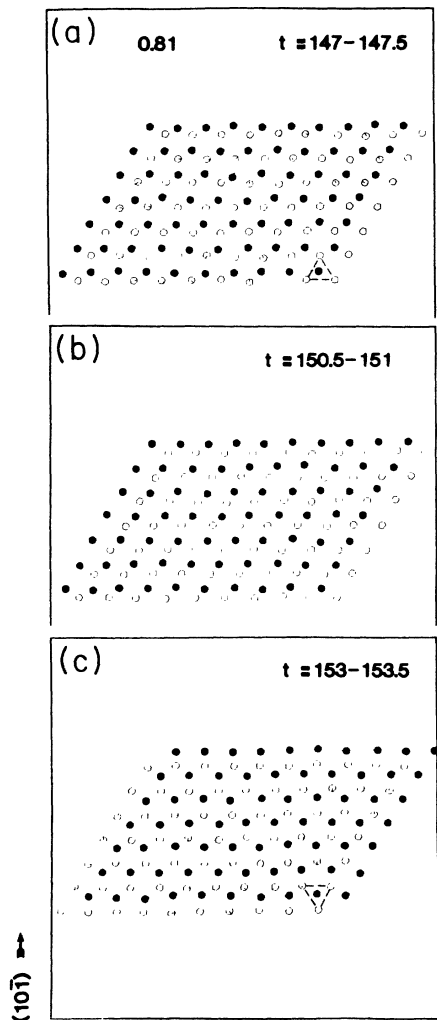


FIG. 5. Details of the system trajectories leading to the formation of a stacking fault. Atoms in layers 12 (solid circles) and 13 (open circles), in the soft material are shown before (a), mid-way through the stacking-fault formation (b), and after the layers have moved to the new registry (c). The atomic trajectories are for a simulation at $\tau_{xz}=0.81$ (as in Figs. 3 and 4).

extra stabilization “pins” this interfacial layer to the hard substrate. The potential energy of the topmost layer of the hard material [layer (9)] is lowered further by about -2.6ϵ . The potential energies of both layers 9 and 10 increase due to the structural transformation. Since the system in this set of calculations is thermally isolated, the structural change is accompanied by a temperature increase as seen from Fig. 7(b) (where the curves for successive layers, starting from 10 and up, are displaced vertically by 0.04ϵ). Note however that the final temperature after the transformation is below the melting temperature for both materials.

The variations of the external stress components for the total system [calculated from Eq. (13), for $\tau_{xz}=0.81$ and using the dynamically determined values of the matrix \underline{H}] are displayed in Fig. 8, versus time. We observe an increase in all components at the time of the structural

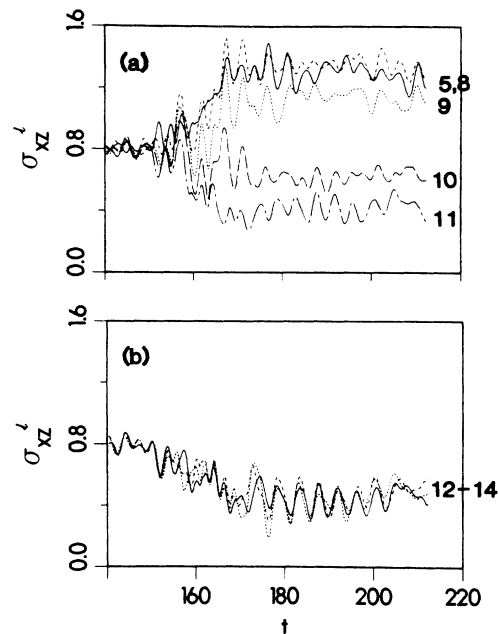


FIG. 6. Per-layer internal stresses (σ_{xz}^l) vs time (in t.u.) for a simulation at $t=0.81$ under adiabatic conditions. Layers 5, 8, and 9 in the hard material and 10 and 11 in the soft material are shown in (a). The stresses in layers 12–14 in the soft material are shown in (b). The interface is between layers 9 and 10. Note the variation in the internal stresses at the time of the structural transformation. The internal stresses in the interior of the soft material (10–14) decrease with layer 10 exhibiting pinning by the hard material. The stress relief in the soft material is accompanied by stress accumulation in the hard material (layers 5–9).

transformation. We also note the axial component, σ_{zz} , in the z direction (along the [111] direction, i.e., normal to the (111) planes) changes character from compressive (due to the initial load on the system) to tensile (positive value) past the structural transformation.

2. Isothermal conditions

To investigate the effect of the ambient thermal conditions we repeated the simulations described in (1) but controlled the temperature of the system, at a reduced temperature of 0.11, via periodic scaling of particle velocities. This system also exhibited structural changes (interlayer slip and stacking-fault generation, but at a higher value of $\tau_s=0.84$, as compared to the value for the adiabatic case ($\tau_s=0.80$). In addition, the volume increase after the transformation was very small. Applying higher values of τ to the system it eventually yielded at a critical value $\tau_c=0.95(\pm 0.01)$, again higher than in the adiabatic case ($\tau_c=0.86\pm 0.02$, see Table I). We conclude that the isothermal system withstands higher values of the external perturbation as compared to the adiabatic case. Since the heat generated during the transformation, which in the adiabatic case can be utilized to overcome potential barriers for structural transformations and

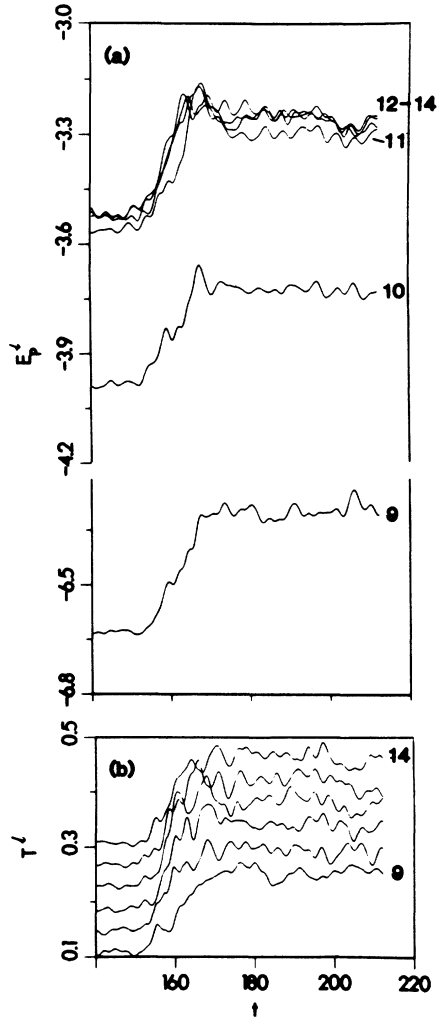


FIG. 7. Per-layer potential energies, E_p^l , in (a), and temperatures, T^l , in (b), for the system simulated at $\tau_{xz}=0.81$ under adiabatic conditions.

yield, is dissipated to the reservoir under isothermal conditions, larger external forces are required in the latter case in order to bring about similar effects.

The behavior versus time of the xz component of the internal stress (σ_{xz}^l) in layers 9–14 at an applied $\tau=0.87$, is shown in Fig. 9. It is seen that while the stresses in layers 10–14 of the soft material vary during the structural transformation they settle to values close to the initial ones. Inspection of the real-space particle trajectories for the system reveals that the system does evolve through deformed structures which contain stacking faults but it does not stabilize in these configurations. Furthermore, in the final state the intralayer registry is intact, which is consistent with the behavior of the internal stresses shown in Fig. 9.

3. The effect of atomic-size mismatch

In the simulations discussed above the materials on both sides of the interface differed by the potential well-depth parameter ϵ ($\epsilon_{BB}=0.5\epsilon_{AA}$), but were character-

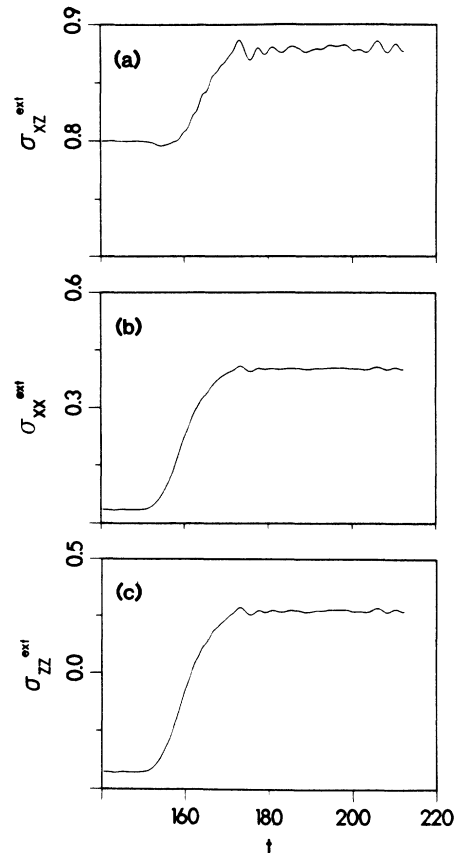


FIG. 8. The external stress components [calculated from Eq. (13)] for simulations at $\tau_{xz}=0.81$ under adiabatic conditions vs time (in t.u.). Increases are observed in all components at the time of structural transformation. Note the change from compressive (due to the initial load) to tensile character in the axial component σ_{zz}^{ext} .

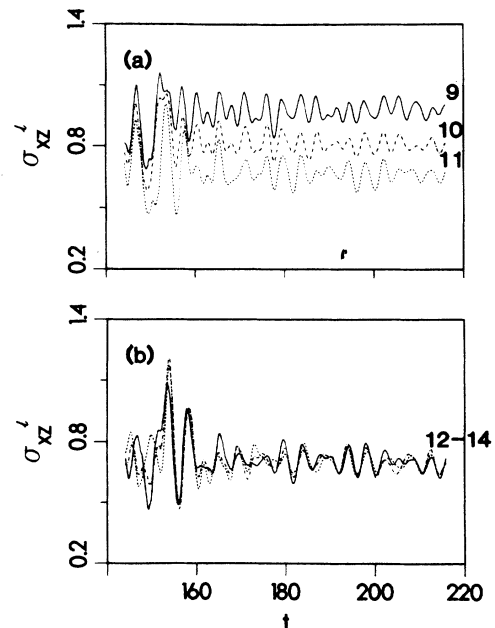


FIG. 9. Per-layer internal stresses (σ_{xz}^l) vs time (in t.u.) for a simulation under isothermal conditions at $\tau_{xz}=0.87$. (a) Layers 9–11; (b) layers 12–14.

ized by the same value of the “atomic-size” parameter, $\sigma_{AA} = \sigma_{BB} = \sigma_{AB}$ [see Eq. (30)]. To investigate the dependence of the system properties on the mismatch in atomic sizes between the two interfacing materials we have performed simulations in which the well-depth parameters were chosen as before (see Sec. III A) but the σ parameters were chosen such that the atoms in the soft (B) material are characterized as having a larger size, i.e., $\sigma_{BB} = 1.5\sigma_{AA}$ and $\sigma_{AB} = 1.25\sigma_{AA}$. In these simulations the hard material (A) occupied six layers (numbered 1–6) and the soft material occupied nine layers (numbered 7–15), with 162 atoms per layer in the A material and 72 atoms per layer in the B (soft) material (the total number of particles was 1620).

A series of studies, similar to those described above, employing the (\mathcal{H}, τ, N) ensemble under thermally adiabatic conditions were performed. From these simulations we have determined that the critical-yield value of the thermodynamic tension in this system is $\tau_{c,xz} = 0.62 \pm 0.01$ (and the corresponding external stress $\sigma_{ec,xz} = 0.51 \pm 0.01$), which are considerably lower than the corresponding values found for the equal-atomic size systems (see Table I). Moreover, unlike the previous cases, where yield was preceded by an external stress regime in which the system responded inelastically via a sequence of structural transformations, for the present system (in which the atomic sizes across the interface differ) no such behavior is observed. Time histories of the layer decomposed potential energy, E_p^l and internal stress, σ_{xz}^l , obtained in a simulation at a constant thermodynamic tension $\tau_{xz} = 0.52$ are shown in Figs. 10 and 11. First we observe that at yield the potential energy and internal stress

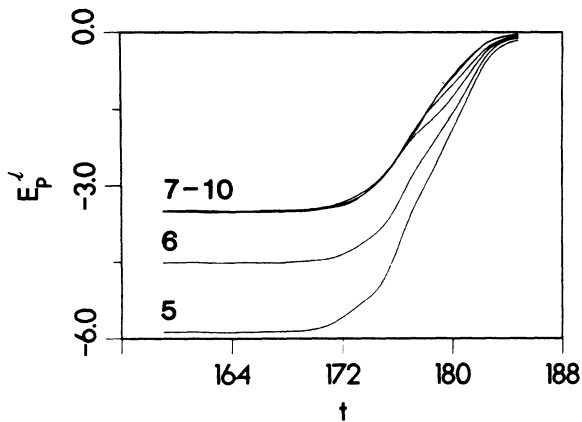


FIG. 10. Per-layer potential energies for a system containing an interface (between layers 6 and 7) between a hard (layers 1–6) and soft (layers 7–15) materials which are characterized in addition by different atomic-size parameters ($\sigma_{BB} = 1.5\sigma_{AA}$). Results are for simulations employing the (\mathcal{H}, τ, N) ensemble, under adiabatic conditions at $\tau_{xz} = 0.52$. Time is in units of t.u. and potential energy in reduced Lennard-Jones units. Note that the whole soft material responds in unison (layers 7–10). The increase in potential energy starting at ~ 172 t.u. corresponds to yield. No distinct structural transformations prior to yield (in contrast to the corresponding equal-atomic-size case discussed previously) were detected.

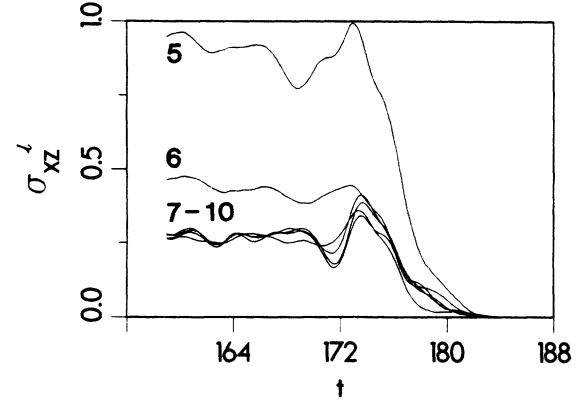


FIG. 11. Per-layer internal stresses in the system described in Fig. 10. Note the stress relief, resulting in yield indicated by the vanishing of the internal stresses.

vanish (stress relief). Secondly we note that the soft system (layer numbers larger than 6) does not exhibit “pinning” by the underlying hard substrate, although the strength of interaction between the two is the same as in the previous studies where such pinning was observed at the interface (see above). Thirdly the whole soft system responds in unison, starting at the interfacial layer and up into the material. These observations can be understood when considering that as a consequence of the larger atomic size the atoms of the soft material at the interface average over the corrugation of the potential due to the substrate, resulting in an effective potential surface which exhibits smaller variations for lateral displacements parallel to the interface plane, and consequently a reduced resistance to shear.

C. Applied strain simulations

We turn next to another mode of simulation in which instead of applying a thermodynamic tension, $\underline{\tau}$, the system is strained while maintaining a constant volume. The preparation of the system up to the application of external forces is the same as described in Secs. III A and III B. The starting point for these simulations is an equilibrium averaged system of 18 layers consisting of nine layers each of hard and soft materials (see Sec. III A), at a reduced temperature $T = 0.11$ under a load of 0.5. (The equilibrium averaged calculational cell is nearly orthogonal with a parallelepiped base with $H_{xx} = 11.04\sigma$, $H_{yy} = 6.69\sigma$, $H_{zz} = 16.25\sigma$, $H_{yz} = 3.86\sigma$, and all other components fluctuating about zero.) At this stage we apply a constant-strain rate $\dot{\underline{\gamma}}$ in the $(11\bar{2})$ plane along the $[110]$ direction (see Fig. 1), i.e.,

$$\dot{H}_{xz} = \dot{\gamma} H_{zz}$$

$$\dot{H}_{\alpha\beta} = 0 \quad (\text{for } \alpha\beta \text{ for which } \alpha \neq x \text{ and } \beta \neq z)$$

with the strain rate $\dot{\gamma} = 4 \times 10^{-3}$ t.u.⁻¹ (i.e., at this strain rate the value of H_{xz} grows from zero to about 30% of H_{zz} in 10^4 integration time steps).

As in the previous simulations (see Sec. III B) we have performed studies under both thermally adiabatic and isothermal conditions. Since the results are similar in both cases we focus on the former ones. Variations of the system temperature, T , and particle potential energy, E_p , versus the strain γ are shown in Fig. 12. As seen these quantities exhibit a characteristic nonmonotonous behavior with an increasing trend. The temperature of the system grows in a stepwise manner and the potential energy in a sawtooth fashion characterized by periods of increase in E_p followed by sharp drops occurring at the same strain values for which the step increases in T occur. To assess possible system size dependencies of the results we display in Fig. 13 similar results for a system in which the number of hard material layers (1–9) is as above but the number of layers of the soft material ($\epsilon_{BB} = \epsilon_{AA}/2$) is doubled (layers 10–27). This system was equilibrated as before and was simulated at a constant-strain rate of $2.8 \times 10^{-3} \text{ t.u.}^{-1}$ (which is equivalent to that used for the smaller system). As evident the overall characteristics of the system temperature and potential energy are similar in both cases, particularly for strains up to and including the first nonmonotonic feature ($\gamma = 0$ to ~ 0.15). Comparison of the systems' response at higher strains indicates that the presence of a larger region of soft material makes the system more pliant. However as we discuss below the overall picture and certain quantitative conclusions are the same for the two system sizes.

To gain further detail about the process underlying the

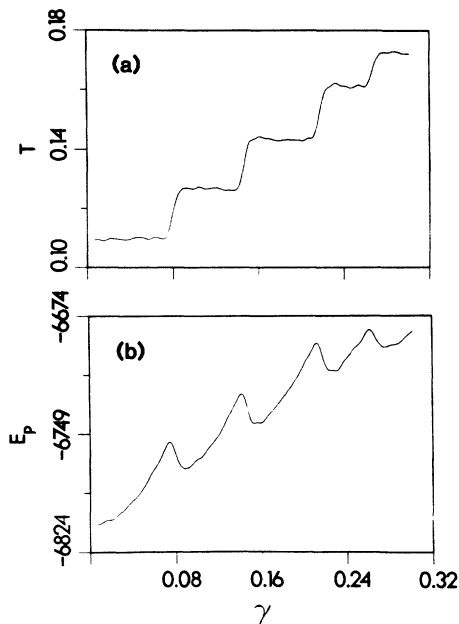


FIG. 12. Temperature (T) and potential energy (E_p) vs strain (γ) for a system composed of 9 layers of hard material and 9 layers of soft material ($\epsilon_{BB} = \epsilon_{AA}/2$), simulated under constant-strain rate ($\dot{\gamma} = 4 \times 10^{-3} \text{ t.u.}^{-1}$) and thermally adiabatic conditions. The steps in the curves are associated with structural transformations. All quantities are given in reduced Lennard-Jones units.

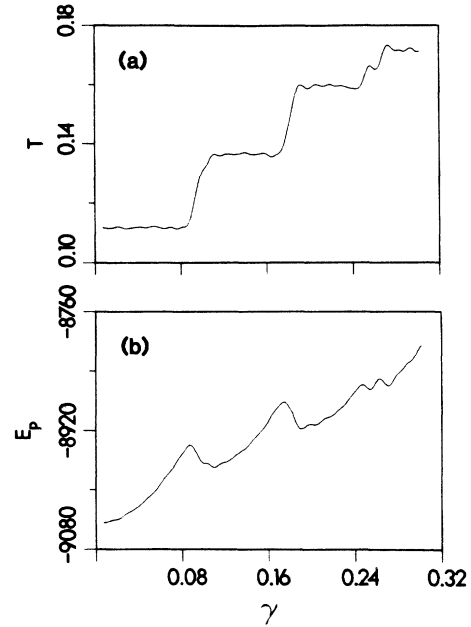


FIG. 13. Same as Fig. 12, but for a larger system size; nine layers of hard material (layers 1–9) and 18 layers of soft material (layers 10–27).

behavior exhibited in Figs. 12 and 13, we display in Figs. 14 and 15 temperature profiles, T^l , decomposed into layers (and offset between layers by 0.03ϵ on the temperature axis) versus strain (γ) for the 18- and 27-layer systems, respectively. As seen the layer temperatures fluctuate in

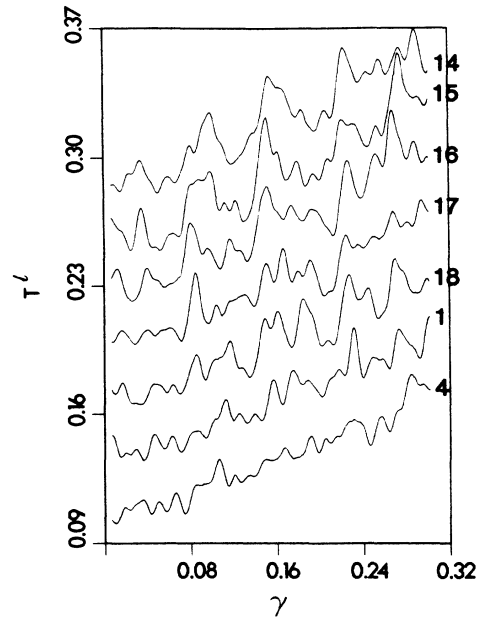


FIG. 14. Per-layer temperatures, T^l , corresponding to the system described in Fig. 12. Note the general heating trend (thermally adiabatic simulations) and the stages of sharp temperature increases, occurring for strain $\gamma \gtrsim 0.08$, in layers 14–18, in the soft material, corresponding to structural transformations.

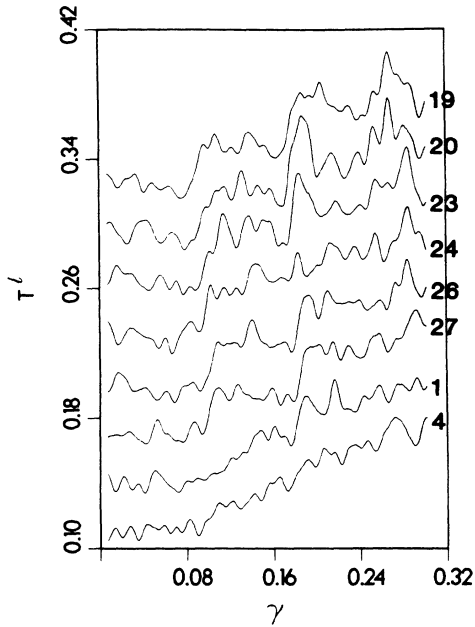


FIG. 15. Same as Fig. 14, for the larger system size (nine layers of hard and 18 layers of soft materials). Note sharp temperature increases in layers 19–27.

response to the applied strain with an overall heating trend. We remind the reader that in the 18-layer system the interface between the hard and soft material is between layers 9 and 10 (and due to the periodic boundary conditions also between 1 and 18), and in the 27-layer system it is located between layers 9 and 10 (and also between layers 1 and 27). A more detailed inspection of Figs. 14 and 15 reveals sharp temperature spikes in regions inside the soft materials (layers 14–18 in Fig. 14 and layers 19–27 in Fig. 15) occurring at characteristic values of the strain which compare with the values of γ at which the nonmonotonic behavior is seen in Figs. 12 and 13. These observations indicate that in response to the applied strain the system deforms by going over potential barriers between structural configurations. In fact examination of the real-space particle trajectories shows that at these characteristic strains interlayer slip is initiated between layers 15 and 16 for the 18-layer system and layers 23 and 24 for the larger one (both inside the soft material in regions removed from the material interface by about 3–5 atomic layers).

To gain further insight about the process of deformation we show in Figs. 16 and 17 layer profiles for the per-layer internal stresses versus strain in the 18- and 27-layer systems, respectively. It is seen that the stress component parallel to the strain direction, σ_{xz} , exhibits a sawtooth shape (much like the potential energies shown in Figs. 12 and 13) with the first peak occurring at $H_{xz} \sim 0.08H_{zz}$ (i.e., at a strain $\gamma = 0.08$). The rises in the stress correspond to stress accumulation and the subsequent drops to stress relief (as corroborated by inspection of real-space particle trajectories which reveal that the stress relief mechanism involves interlayer slip). The os-

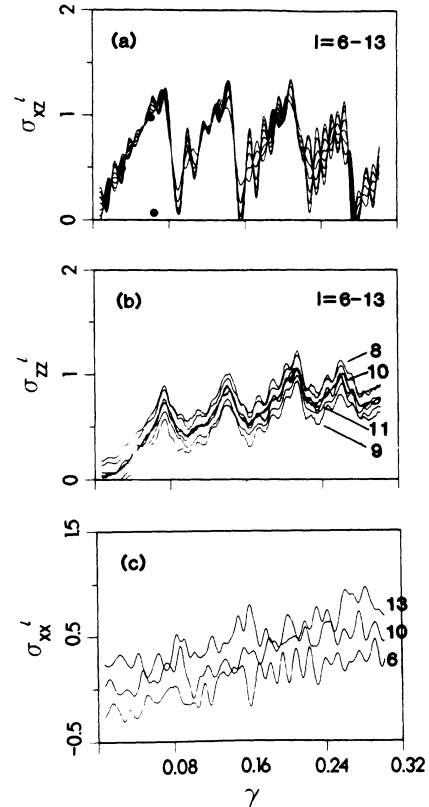


FIG. 16. Per-layer internal stress vs strain (γ) profiles for the σ_{xz}^l [in (a)], σ_{zz}^l [in (b)], and σ_{xx}^l [in (c)], components for the system composed of nine layers of hard and nine layers of soft material, and simulated under adiabatic conditions. Note the monotonic increases in internal stress in σ_{xz}^l and the axial component σ_{zz}^l followed by sharp drops corresponding to structural transformations. The solid dots in (a) give the values of the internal stress component σ_{xz}^l obtained via constant strain simulations at the corresponding values of γ . As seen, for values of $\gamma < 0.063$ (first two dots) the values of σ_{xz}^l thus obtained coincide with those corresponding to the constant strain rate simulations. For $\gamma = 0.063 \pm 0.002$ the internal stress drops sharply, corresponding to a structural stress relieving transformation in the system. The constant-strain simulations were used to determine the critical stresses given in Table I. All quantities are in reduced Lennard-Jones units.

cillatory behavior seen in Figs. 16(a) and 17(a) after the slip is due to damped planar oscillations in the new structural configuration. The same general behavior is seen for the axial stress component, σ_{zz} (i.e., the stress component along the [111] direction [see Figs. 16(b) and 17(b)]). Note that for σ_{zz} the curves are bunched in groups with the interfacial layers (8, 10, and 9, 11) bounding the closely-packed stress curves corresponding to the middle region in the hard and soft materials (layers 6, 7 and 12, 13 for both system sizes). Finally, the axial stress component σ_{xx} , in the direction $[1\bar{1}0]$ of the applied strain, shown in Figs. 16(c) and 17(c), exhibits merely fluctuations with a rising trend [also seen for σ_{zz} , see Figs. 16(b) and 17(b)] which is a direct consequence of the

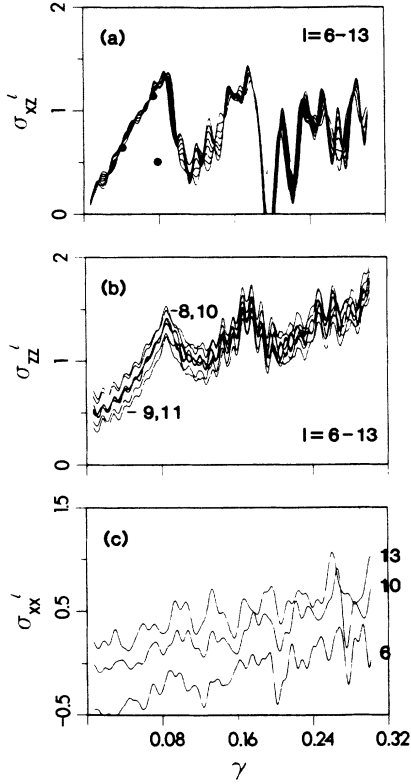


FIG. 17. Same as Fig. 16, but for the larger system, composed of nine layers of hard material and 18 layers (10–28) of soft material.

heating of the system. Note in addition the transition from compressive (due to the initial load) to tensile behavior as the strain increases. The difference between the character of variations in σ_{xx} (similarly σ_{yy}) and that of σ_{xz} and σ_{yz} is consistent with our observation that the stress relief mechanism is via processes in which (111) planes slip past one another with no significant intralayer distortions.

As already mentioned in Sec. III B the rate of application of the perturbation [applied shear stress (or thermodynamic tension) as discussed in Sec. III B and applied strain in this section] in MD simulations is faster than laboratory rates. In addition these rates are also too fast to allow an adiabatic (in the sense of dynamical relaxation on the atomic scale) response of the system. With regard to the first issue we refer to the studies of Moran, Ladd, and Hoover²⁸ who suggested on the basis of comparison between NEMD simulations and experiments that large-deformation and plastic-flow phenomena in close-packed metals obey a scaling relation which allows comparison between MD calculations and experimental data although the two differ by orders of magnitude in the rates of the applied shear. Moreover these authors suggest that these observations imply that plastic response and flow of these metals can be described by a single physical mechanism over a range of strain rates from 10 kHz to 1 THz (our values of $\dot{\gamma}$ using well depth, ϵ , and σ parameter values in the 6–12 LJ potential to ap-

proximate typical metals, are of the order of 10 GHz).

To address the second issue and determine accurately temporally adiabatic values for the critical strains (i.e., those at which inelastic structural deformations occur) in our system, we have performed for both system sizes simulations at constant strains approaching the value at which slip occurred [see first peak in Figs. 16(a) and 17(a) at $\gamma \sim 0.08$]. Thus in these series of simulations the system was allowed to fully relax under prescribed strains. The values for the internal stresses, σ_{xz} , obtained from these simulations are represented by solid dots in Figs. 16(a) and 17(a). First we note that for strains below the critical strain value the developed internal stresses in these simulations are the same as those obtained in the constant-strain-rate studies, which indicates that for this regime of strain values the system responds adiabatically even when the strain is applied at a rather high rate. Secondly, the values of the critical strain, γ_s obtained in these simulations (see Table I, $\gamma_{s,xz} = H_{xz}/H_{zz} = 0.063 \pm 0.002$ for the 18-layer system and 0.076 ± 0.002 for the 27-layer system) are below that given by the constant-strain-rate simulations. Thirdly, the corresponding values of the internal stresses $\sigma_{s,xz}$ (0.975 and 1.14 for the small and large system, respectively, see Table I) are larger than the one obtained using the adiabatic (\mathcal{H}, τ, N) simulations (Sec. III B), and the one for the 27-layer system is somewhat higher than that of the smaller system. Note however, that the critical strain-to-stress ratio, γ_s/σ_s is nearly the same for both systems (0.0634 and 0.0652, for the small and large systems, respectively). We conclude therefore that while the larger system exhibits a somewhat larger tolerance to strain (i.e., is more pliant) the elastic properties of our systems are independent of thickness at or above nine layers of soft material. Finally, we note that for strain values above γ_s , the systems exhibit slip accompanied by sharp drops in the value of the internal stress σ_{xz} (and similarly for σ_{zz}) indicating stress relief. We note that removing the strain for strain values below the critical value γ_s , results in a return of the system to the unstrained configuration, indicating that in this strain regime the system deforms elastically, while after removing the strain past the structural transformation (i.e., for values larger than γ_s) the system remains in the new structural configurations.

IV. SUMMARY

In this investigation we have studied the formulations of molecular-dynamics techniques for simulations of material systems evolving under applied finite external perturbations. Methodologies of simulations of phenomena involving finite deformations (plastic deformations, structural transformations, yield, and flow) have been discussed (Sec. II) and demonstrated (Sec. III). These simulations yield valuable information about the atomic scale mechanisms of materials' dynamical response to mechanical perturbations.

In these studies we focused on interfacial systems, composed of interfacing crystalline solids characterized by differing interatomic interaction strengths and in some

cases also by differing atomic sizes. Our main results may be summarized as follows.

(i) For interfacial systems which are characterized by differing interatomic interaction strengths (i.e., the interface is between a hard and soft material), the system responds to an applied nonisotropic perturbation (applied shear or strain) first elastically and then via stress relief mechanisms which involve structural transformations (stacking-fault formation and interlayer slip). For larger values of the external forces, eventual yield occurs.

(ii) Critical values of the external perturbation required in order to bring about inelastic response (structural transformations and yield) have been determined (see Table I). Our simulations demonstrate that these critical values are smaller for a system under thermally adiabatic conditions than for an isothermal environment. The origin of the difference lies in the dissipation of the generated thermal energy under isothermal conditions, which necessitates larger values of the external perturbations in order to overcome potential barriers for structural modifications and eventual yield.

(iii) The cohesive interatomic interactions at the interface between a hard substrate and a soft material result in "pinning" of the soft material at the interface (1–3 atomic layers). As a result the response of the system to the external perturbation (stress relief via plastic as well as structural transformations) occurs in a "shear band" consisting of a few atomic layers inside the soft material, which are located at about 1–3 layers away from the original (unstressed) interface. The stress relief in the soft material is accompanied by stress accumulation in the

hard substrate.

(iv) MD simulations for interfacing hard and soft materials, which in addition are characterized by differing atomic sizes, reveal the important role played by atomic-size mismatch in determining the atomic-scale mechanism of response. For such system it was found that no adhesive pinning occurs at the interface, and that the soft (and larger atomic size) material responds as a whole with no distinct structural transformations preceding the yield point. The critical-yield stress value for this system is significantly lower than that found for the corresponding equal-atomic-size system.

(v) Comparison of our results in this study for the [111] interface with our previous investigations of the [100] interface¹⁷ demonstrates the dependence of the critical values of the shear stresses on the crystallographical orientation of the interface, as well as of certain details of the stress relief mechanisms.

ACKNOWLEDGMENTS

This work is supported by the Hughes Aircraft Company, under the Defense Advanced Research Projects Agency (DARPA)–Hughes Tribological Fundamentals Program, DARPA Order No. 5177, U.S. Air Force Wright Aeronautical Laboratory (AFWAL) Contract No. F33615-C-5087 and by the U.S. Department of Energy (DOE) under Grant No. DE-FG05-86ER-45234. Most of the calculations were performed at the Pittsburgh Supercomputer Center.

¹L. Davison, *Mater. Res. Soc. Bull.* **8**, 14 (1988); see also *Approaches to Modeling of Friction and Wear*, edited by F. F. Ling and C. H. T. Pass (Springer, Berlin, 1988).

²U. Landman, in *Computer Simulation Studies in Condensed Matter Physics: Recent Developments*, edited by D. P. Landau and H. B. Schutter (Springer, Berlin, Heidelberg, 1988); see also other articles in this volume.

³U. Landman *et al.*, *Mater. Res. Soc. Sym. Proc.* **63**, 273 (1985); see also other articles in this volume.

⁴F. F. Abraham, *Adv. Phys.* **35**, 1 (1986); *J. Vac. Sci. Technol. B* **2**, 534 (1984).

⁵*Mater. Res. Soc. Bull.* **XIII** (2), 14–39, February 1988.

⁶U. Landman, R. N. Barnett, C. L. Cleveland, J. Luo, D. Scharf, and J. Jortner, in *Proceedings of the Symposia of the Topical Group on Few-Body Systems and Multiparticle Dynamics*, AIP Conf. Proc. No. 162, edited by D. A. Micha (AIP, New York, 1987), p. 200.

⁷D. W. Heerman, *Computer Simulation Methods* (Springer, Berlin, 1986).

⁸*Computer Simulations of Solids*, edited by C. R. A. Catlow and W. C. Machord (Springer, Berlin, 1982).

⁹W. G. Hoover, *Molecular Dynamics*, Vol. 258 of *Lecture Notes in Physics* (Springer, Berlin, 1986).

¹⁰H. C. Andersen, *J. Chem. Phys.* **72**, 2384 (1980).

¹¹M. Parrinello and A. Rahman, *J. Appl. Phys.* **52**, 7182 (1981).

¹²J. R. Ray and A. Rahman, *J. Chem. Phys.* **80**, 4423 (1984).

¹³For an extension to metallic systems see R. N. Barnett, C. L.

Cleveland, and U. Landman, *Phys. Rev. Lett.* **54**, 1679 (1985); **55**, 2035 (1985).

¹⁴W. G. Hoover, *Phys. Rev. A* **118**, 111 (1983).

¹⁵See reviews by S. Yip and M. Parrinello, in *Molecular-Dynamics Simulations of Statistical-Mechanical Systems*, Proceedings of the International School of Physics, "Enrico Fermi," Course XCVII, Varenna, 1985, edited by C. Ciccotti and W. G. Hoover (Societe Italiane di Fisica, Bologna, 1986).

¹⁶See recent reviews by D. J. Evans and G. P. Morriss, *Comput. Phys. Rep.* **1**, 297 (1984); D. J. Evans and W. G. Hoover, *Ann. Rev. Fluid Mech.* **18**, 243 (1986).

¹⁷M. W. Ribarsky and U. Landman, in *Approaches to Modeling of Friction and Wear*, edited by F. F. Ling and C. H. T. Pan (Springer-Verlag, New York, 1988), p. 159.

¹⁸S. Sutton, M. W. Ribarsky, and U. Landman, *J. Chem. Phys.* (to be published).

¹⁹C. L. Cleveland, *J. Chem. Phys.* (to be published).

²⁰G. J. Dienes and A. Paskin, in *Atomistic of Fracture*, edited by R. M. Latanision and J. R. Pickens (Plenum, New York, 1983), p. 671; A. Paskin, K. Sieradzki, D. K. Som, and G. J. Dienes, *Acta Metall.* **31**, 1253 (1983).

²¹B. DeCelis, A. S. Argon, and S. Yip, *J. Appl. Phys.* **54**, 4864 (1983), and references therein.

²²W. T. Ashurst and W. G. Hoover, *Phys. Rev. B* **14**, 1465 (1976).

²³W. G. Hoover, N. E. Hoover, and W. C. Moss, *J. Appl. Phys.* **50**, 829 (1979); see also A. J. C. Ladd and W. G. Hoover,

- Phys. Rev. B **26**, 5469 (1982).
- ²⁴P. C. Gehlan, G. T. Hahn, and M. F. Kanninen, *Scr. Metall.* **6**, 1087 (1972).
- ²⁵See review by M. I. Baskas and M. S. Daw in *Computer Simulations in Materials Science*, edited by R. J. Arsenault, J. Beeler, and D. M. Esterling (American Society for Metals, Cleveland, 1988).
- ²⁶R. Najafabadi and S. Yip, *Scr. Metall.* **17**, 1199 (1983).
- ²⁷J. R. Ray and A. Rahman, *J. Chem. Phys.* **82**, 4243 (1985).
- ²⁸B. Moran, A. J. C. Ladd, and W. G. Hoover, *Phys. Rev. B* **28**, 1756 (1983).
- ²⁹B. L. Holian, *Phys. Rev. A* **37**, 2562 (1988).
- ³⁰M. D. Kluge, J. R. Ray, and A. Rahman, *J. Chem. Phys.* **85**, 4028 (1986); M. D. Kluge and J. R. Ray, *Phys. Rev. B* **37**, 4132 (1988).
- ³¹F. D. Murnaghan, *Finite Deformations of an Elastic Solid* (Wiley, New York, 1951).
- ³²R. N. Thurston, in *Physical Acoustics*, edited by W. P. Mason (Academic, New York, 1964), Vol. 1, Pt. A.
- ³³H. Goldstein, *Classical Mechanics* (Addison-Wesley, Reading, Mass., 1950).
- ³⁴This interface orientation was chosen in view of our previous studies of the [001] interface (see Ref. 17), where it was found that slip occurs for the Lennard-Jones fcc system along the (111) planes. Note that the values for external stress given in Ref. 17, should be interpreted as those for the thermodynamic tension (see Sec. II).
- ³⁵If the interaction parameters are chosen such that they correspond to the cohesive energy and lattice constant of nickel ($\epsilon = 3.54 \times 10^{-13}$ erg, $\sigma = 2.49$ Å, and atomic mass $m = 9.75 \times 10^{-23}$ g) a reduced temperature $T = 0.11$ corresponds to 300 K, the reduced melting temperature $T_m = 0.7$ corresponds to 2000 K, the reduced unit of stress or load to 2.4×10^7 g/cm² (or 2.4×10^{10} dyn/cm²), and the reduced time unit (t.u.) corresponds to 4.1×10^{-13} sec.